Unconventional Air-Stable Interdigitated Bilayer Formed by 2,3-Disubstituted Fatty Acid Methyl Esters

**Xiaodong Chen,[†] Susanne Wiehle,[‡] Markus Weygand,[§] Gerald Brezesinski,[§] Ute Klenz,[‖]
Hans-Joachim Galla,[‖] Harald Fuchs,[†] Günter Haufe,*,[‡] and Lifeng Chi*,[†]**

*Physikalisches Institut, Westfälische Wilhelms-Universität, Wilhelm-Klemm-Str. 10, 48149 Münster, Germany,
Center for Nanotechnology (CeNTech), Gievenbeckweg 11, 48149 Münster, Germany, Organisch-Chemisches
Institut, Westfälische Wilhelms-Universität, Corrensstrasse 40, 48149 Münster, Germany, Max Planck Institute
of Colloids and Interfaces, 14424 Potsdam, Germany, and Institut für Biochemie, Westfälische Wilhelms-
Universität, Wilhelm-Klemm-Str. 2, 48149 Münster*

A single-chain fatty acid methyl ester, racemic *anti*-3-fluoro-2-hydroxyeicosanoic acid methyl ester (β-FHE),
forms an unconventional air-stable interdigitated bilayer at the air−water interface. The interdigitated bilayer
transferred onto solid substrate by the Langmuir−Blodgett (LB) technique keeps air-stable without any substrate
modification or protein inclusion. There are two visible plateaus in the surface pressure−molecular area (π−
A) isotherms of β-FHE Langmuir film during continuous compression. According to Brewster angle microscopy
(BAM), grazing incidence X-ray diffraction (GIXD), X-ray reflectivity (XR), fluorescence microscopy (FM),
and atomic force microscopy (AFM) measurements, the first plateau is attributed to the coexistence of liquid
expanded (LE) and liquid condensed (LC) phases in the monolayer, while the second plateau is interpreted
as the transition from LC monolayer to interdigitated bilayer. The coupling between tilt and curvature associated
with the packing mismatch between headgroup and chain gives rise to buckling and folding of the monolayer,
leading to the transition of the LC monolayer to a bilayer structure. The diffusion-limited aggregation (DLA)
model is applied to describe the formation of the fractal structures of the bilayer as observed in the second
plateau. In addition, the transition between monolayer and bilayer is reversible. The present works are interesting
for understanding biological processes, for example, the behavior of lung surfactants.

1. Introduction

Lipid bilayer structures play a crucial role in biological cell membranes and are interesting for chemists and physicists to study basic questions of surface science. Artificial lipid bilayers on different supported matrixes, mostly prepared by fusing vesicles,[1,2] can serve well as cell membrane mimics that possess the unique combination of physical and biological properties, which are very important for biosensors[3] and nanodevices.[4] The fully hydrated, supported lipid bilayers, however, are quickly destroyed when exposed to air. Several methods, such as preparation of hybrid bilayers,[5] photopolymerized crossed-linked membranes,[6−8] substrate modifications,[9] and protein binding protection,[10,11] have been used to overcome this limitation. In addition, until now, most of the supported bilayers were fabricated by double-tailed phospholipids.

A spontaneous multilayer film formation at the air−water interface has often been observed for molecules containing hydrogen bonding groups at both ends of the chain, as well as for pure long-chain alkanes.[12] Also, multilayer formation can be obtained by compressing a Langmuir monolayer film (Figure 1a) beyond its collapse point.[13−15] Most of them form a stable
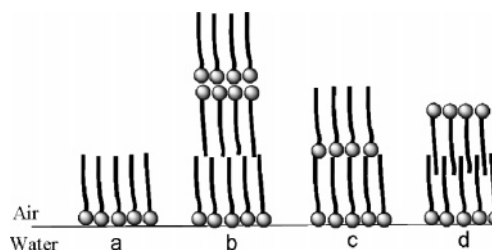
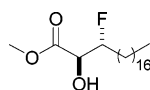* Corresponding authors. E-mail: haufe@uni-muenster.de (G.H.);
chi@uni-muenster.de (L.C.)..
† Physikalisches Institut, Westfälische Wilhelms-Universität.
‡ Organisch-Chemisches Institut, Westfälische Wilhelms-Universität.
§ Max Planck Institute of Colloids and Interfaces.
‖ Institut für Biochemie, Westfälische Wilhelms-Universität.

Figure 1. Schematic representations of various Langmuir film structures at the air−water interface: (a) a typical Langmuir monolayer; (b) a "head-to-head" bilayer on the top of a monolayer; (c) a "head-to-tail" bilayer; and (d) a "tail-to-tail" interdigitated bilayer.

"head-to-head" bilayer on the top of a monolayer (Figure 1b) or a "head-to-tail" bilayer (Figure 1c) at the air−water interface. Only a few of them form "tail-to-tail" interdigitated bilayers[13] (Figure 1d), which resemble the structure of the natural membranes. Normally, because of the high energy of the hydrophilic top layer, the "tail-to-tail" bilayer exposed to air is quickly destroyed and buckles to form multilayers. However, through weak acid−base interaction between the headgroups in binary mixtures of amphiphiles,[13] it is still possible to obtain "tail-to-tail" bilayers. Normally, such a bilayer is obviously amorphous, for which no grazing incidence X-ray diffraction (GIXD) peaks were observed.

Here, we report on an unconventional air-stable interdigitated bilayer formed at the air−water interface by a single-chain fatty acid methyl ester, racemic *anti*-3-fluoro-2-hydroxyeicosanoic

Bilayer Formed by Fatty Acid Methyl Esters

J. Phys. Chem. B, Vol. 109, No. 42, 2005 **19867**

CHART 1

Figure 2. (Left) $\pi-A$ isotherm and a sequence of typical BAM images of β-FHE Langmuir film at the air−water interface at 20 °C. Scale bars for BAM are 100 μm. Inset shows schematic structures (LC monolayer and interdigitated bilayer) of the β-FHE Langmuir film. The arrows show the states at which GIXD patterns were recorded (see Figure 4).

acid methyl ester (β-FHE) (Chart 1). What makes this system interesting and different from other examples of supported bilayers[5−11] is the fact that the bilayer is formed only by one component of a single-chain fatty acid methyl ester and the interdigitated bilayer is air-stable without any substrate modification or protein inclusion. In addition, the transition between monolayer and bilayer is reversible. The present work would be interesting to understand biological processes, for example, the behavior of lungs, which involves a coexistence of two-dimensional (2D) and three-dimensional (3D) structures of lung surfactant at the aqueous−air interface.[16,17]

2. Results and Discussion

$\pi-A$ Isotherm and Brewster Angle Microscopy Measurements. Figure 2 shows a surface pressure−molecular area ($\pi-A$) isotherm and Brewster angle microscopy (BAM) images of a β-FHE Langmuir film at the air−water interface at 20 °C. Notably, there are two visible plateaus for this Langmuir film during continuous compression. The first plateau is attributed to the phase transition from a liquid-expanded (LE) phase to a liquid-condensed (LC) phase, which is confirmed by BAM images (a and b of Figure 2), and it follows the general rule of the LE−LC transition (e.g., the surface pressure of the plateau increases with increasing temperature). Before the second plateau, a homogeneous LC monolayer is formed (BAM image d of Figure 2), and the corresponding extrapolated molecular area is 34 Å^2, which is much bigger than that of normal fatty acid esters (∼20 Å^2). This might be due to the large 2,3-disubstituted headgroup of β-FHE. The isotherm reaches the second plateau after an inflection point at $A \sim 25$ Å^2. It is interesting to note that, at the beginning of the second plateau region, some small domains appear (e of Figure 2), although the LC monolayer covers the whole water surface. This suggests that a second condensed phase appears above the first condensed layer. Upon gradual compression, the domains grow homogeneously within the second plateau region of the isotherm (f and g of Figure 2), which implies a homogeneous thickness of the second layer. The surface pressure of the second plateau decreases with increasing temperature, which supports the assumption that this plateau region is rather the monolayer collapse, and not an LC1−LC2 transition. Moreover, we observe that the collapse pressure varies linearly with the logarithm of the compression rate, as shown in Figure 3. This behavior is typical for monolayer collapse processes.[18−22] The last feature of the second plateau is that the isotherm displays a third rise at the end of the second plateau with the molecular area of ∼13 Å^2, which is half of the area at the beginning of the second plateau. This further supports the assumption that the domains at the second plateau are bilayers and brings two major questions: (1) How does the LC monolayer transform to a bilayer? (2) Which kind of bilayer structure is formed: a "head-to-tail" bilayer, or a "tail-to-tail" interdigitated bilayer?

GIXD Measurement. GIXD patterns were measured at different points along the $\pi-A$ isotherm to elucidate the structural information at the air−water interface with subnanometer resolution. Selected contour plots, taken at pressures marked by arrows in the $\pi-A$ isotherm (Figure 2), are shown in Figure 4. Instead of well-defined Bragg peaks, the scattered intensity distributes on an arc. Assuming a constant tilt of
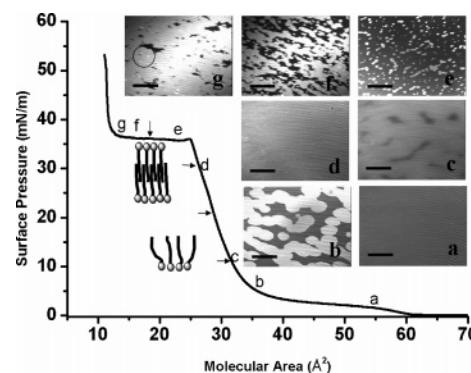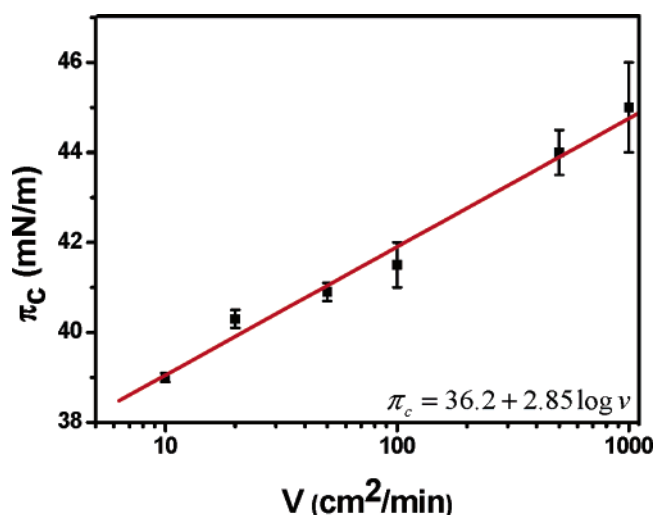

Figure 3. Dependence of the collapse pressure (π_c) on the compression rate (v) at 20 °C.

molecules and a constant packing density within the monolayers, the intensity distribution shows that the tilt direction (tilt azimuth) changes continuously from NN (nearest neighbor tilt) to NNN (next nearest neighbor tilt). This means that different lattice structures (orthorhombic with different tilt directions and oblique with intermediate tilt directions) are present in the monolayer at the same time. The reason could be the mismatch between the area requirement of headgroup and chain. On the basis of the assumption that we can determine the extreme cases of NN and NNN tilted rectangular unit cells, we find the positions of the nondegenerated and degenerated peaks for these two lattices. The corresponding structural parameters for β-FHE Langmuir films are shown in Table 1. The tilt angle decreases from 40° at ∼10 mN/m to 32° at ∼30 mN/m, and the cross-sectional area is approximately 20.5 Å^2. At the second plateau region, an additional Bragg peak at 1.52 Å^{-1} ($d = 4.13$ Å) appears. If we assume that this peak represents a hexagonal lattice of nontilted molecules (the peak is located at zero Q_z), then the cross-sectional area is 19.7 Å^2. This packing is much tighter compared to that of the monolayer and could be an indication for an interdigitated phase allowing tighter packing of chains irrespective of a large headgroup.

X-ray Reflectivity Measurement. X-ray reflectivity (XR) measurements show that a homogeneous monolayer is formed
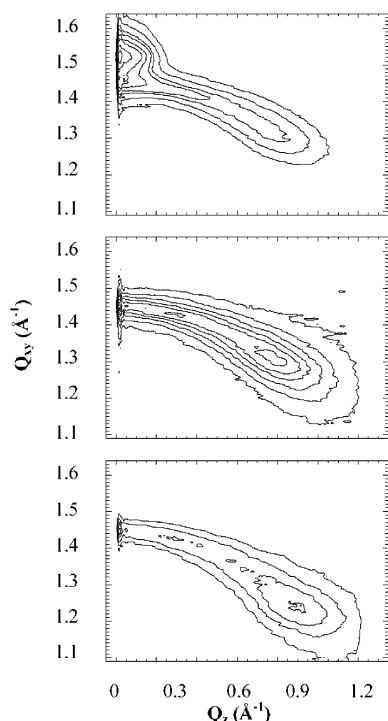
Figure 4. Selected contour plots of the corrected X-ray intensities as a function of the in-plane scattering vector component Q_{xy} and the out-of-plane scattering vector component Q_z at different pressures. From bottom to top: 19.8 mN/m; 29.8 mN/m; and the second plateau region (18 Å^2/molecule, 36.0 mN/m. The real pressure at this point is 31.3 mN/m because the pressure was quickly decreasing to and remained at 31.3 mN/m when we stopped the barrier in order to obtain the data.)

after the first plateau. An electron density distribution along the surface normal of the β-FHE monolayer (9.8 mN/m) at the air–water surface, as shown in Figure 5, was obtained by a model-free inversion of the reflectivity data.[23] Using the molecular area of a β-FHE molecule (27 Å^2) determined from GIXD diffraction data (20.5/cos 40°), one determines the value for the full width at half maximum (fwhm) of the chain electron density distribution to be 17.6 Å, which translates directly to the length of the tail. Assuming an all-trans conformation of the chains, the length of the hydrophobic chain can be calculated (~22.7 Å). Comparing these two values gives a tilt angle of approximately 39°, which is consistent with the GIXD data. This result is also in agreement with the headgroup arrangement in the most stable conformers of β-FHE in solution and in the gas phase.[24] The conformation is rather different from the ideal zig-zag form of the chain. The reflectivity curve taken at the second plateau is completely different (Figure 5), showing qualitatively an increasing thickness. Because the system is a mixture of a mono- and a bilayer of unknown coverage and not evident coherent or incoherent superposition of the fields, this reflectivity curve was not inverted into an electron density profile.

Fluorescence Microscopy Measurements. Fluorescence microscopy (FM) images of β-FHE Langmuir film compressed at 20 °C are presented to provide more insight into phase separation processes, domain morphology, domain growth, collapse processes, and collapse structures. Figure 6 shows FM images of the Langmuir film morphology at various points along the isotherm. Compression of the monolayer, initially in the gas (G) and G–LE coexistence phase, leads to a uniform LE phase (a of Figure 6). Further compression of the monolayer resultes in the nucleation and growth of LC phase domains (b–f of Figure 6) between 32 and 55 Å^2. The LE–LC biphasic

domain structures disappear, and a homogeneous LC monolayer is formed below 30 Å^2 (h and i of Figure 6). This result is consistent with BAM measurements. When the film is compressed to the beginning of the second plateau crossing the inflection point, small bright circular domains appear (j of Figure 6), which should correspond to the collapsed domains. Obviously, there are more fluorescent dye molecules within the circular domains compared to the underlying monolayer. Upon gradual compression at the second plateau, the domains grow and form fractal structures, which surround the bright circular nucleic domains (k–o of Figure 6). The boundary between the fractal structures becomes brighter, which might be attributed to the "less order" state in the boundary region compared with that in the fractal structures. The dark domains, attributed to the multilayers (more than bilayer), appear after the second plateau (p of Figure 6), which can also be observed in the BAM image (brighter dots in g of Figure 2). Confocal laser scanning microscope (CLSM) measurements also confirm the formation of fractal structure (Figure 7).

Atomic Force Microscopy Measurements. Atomic force microscopy (AFM) was used to measure the film transferred onto mica by the Langmuir–Blodgett (LB) technique to obtain the information about morphology, structure, thickness, and surface properties. From the defects of the monolayer film transferred at a surface pressure of 4 mN/m (Figure 8a), we obtain a thickness of about 1.2 nm, which is smaller than the result of XR measurement. However, the reduced thickness is a normal case for organic layer and biomolecular assemblies measured by tapping AFM due to the tip–sample interactions.[25,26] Moreover, in the LC domain, striped structures with the height difference of ~0.4 nm are observed (Figure 8a). This could be due to two kinds of different lattice structures with different tilt angle in the LC domains, which is consistent with the results of GIXD measurements shown above. Also, even for the monolayer transferred at 32 mN/m, we still can see striped domains (Figure 8b), although the height difference becomes smaller. This behavior is similar to previous results[27] of fatty acid methyl and ethyl esters that easily form striped structures in the monolayer due to nonuniform tilt angle of the chains, which is a result of the minimum-energy configuration depending on the mismatch of headgroups and chains.

When the film is transferred at the beginning of the second plateau crossing the inflection point, smaller dots are observed (as arrow shown in Figure 9a) and the height difference is found to be about 1.8 nm. So, the smaller dots could be attributed to the initiation of collapse structures. Meanwhile, we found that there are several circular domains in which smaller dots are located in the center of a domain. The circular domains and other regions (Figure 9a) both are monolayers, and the only difference is the density of the molecules. Upon gradual compression at the second plateau, the dots grow to fractal structures (Figure 9b), which are consistent with FM results at the air–water interface. Further, a part of the fractal structure are observed by AFM measurements for the film transferred onto mica at $A = 18$ Å^2. We found a homogeneous thickness of domain (~2 nm, from the height profile of Figure 10a) that further confirms the BAM results shown above. From BAM measurements, we already know that the first monolayer film is homogeneous, so we think that 2 nm is the height difference between the top layer and the bottom monolayer. Moreover, the phase image of SFM (Figures 9b and 10b) shows that the surface of the top layer is different from the surface of the bottom monolayer, which is an indication for a "tail-to-tail" bilayer structure (Figure 1d) in the second plateau region and on the mica surface.

TABLE 1: Peak Positions of β-FHE Langmuir Films at Different Pressures at the Air−Water Interface[a]

		peak 1		peak 2		peak 3		peak 4		peak 5				
π	A	Q_{xy}	Q_z	Q_{xy}	Q_z	Q_{xy}	Q_z	Q_{xy}	Q_z	Q_{xy}	Q_z	t	A_{xy}	A_0
9.8	32	1.185	1.00	1.375	0.50	1.450	0	1.250	0.85			40.0	26.8	20.5
19.8	29	1.225	0.90	1.400	0.45	1.450	0	1.300	0.79			36.2	25.4	20.5
29.8	26	1.285	0.82	1.420	0.41	1.450	0	1.335	0.72			32.6	24.3	20.4
31.3[b]	18	1.290	0.81	1.420	0.40	1.460	0	1.340	0.70	1.520	0	32.0	24.2	20.4

[a] π: surface pressure (mN/m). A: molecular area (Å²/molecule). Q_{xy}: in-plane scattering vector component (Å⁻¹). Q_z: out-of-plane scattering vector component (Å⁻¹). A_{xy}: in-plane area (Å²). A_0: cross-sectional area (Å²). t: Tilt angle of the alkyl chains from the normal to the air−water interface (deg). Peak 1 and peak 2 are attributed to NNN; and peak 3 and peak 4 are attributed to NN. [b] The real pressure at plateau region is 36 mN/m. The pressure was quickly decreasing to 31.3 mN/m during the GIXD measurement due to bilayer relaxation.
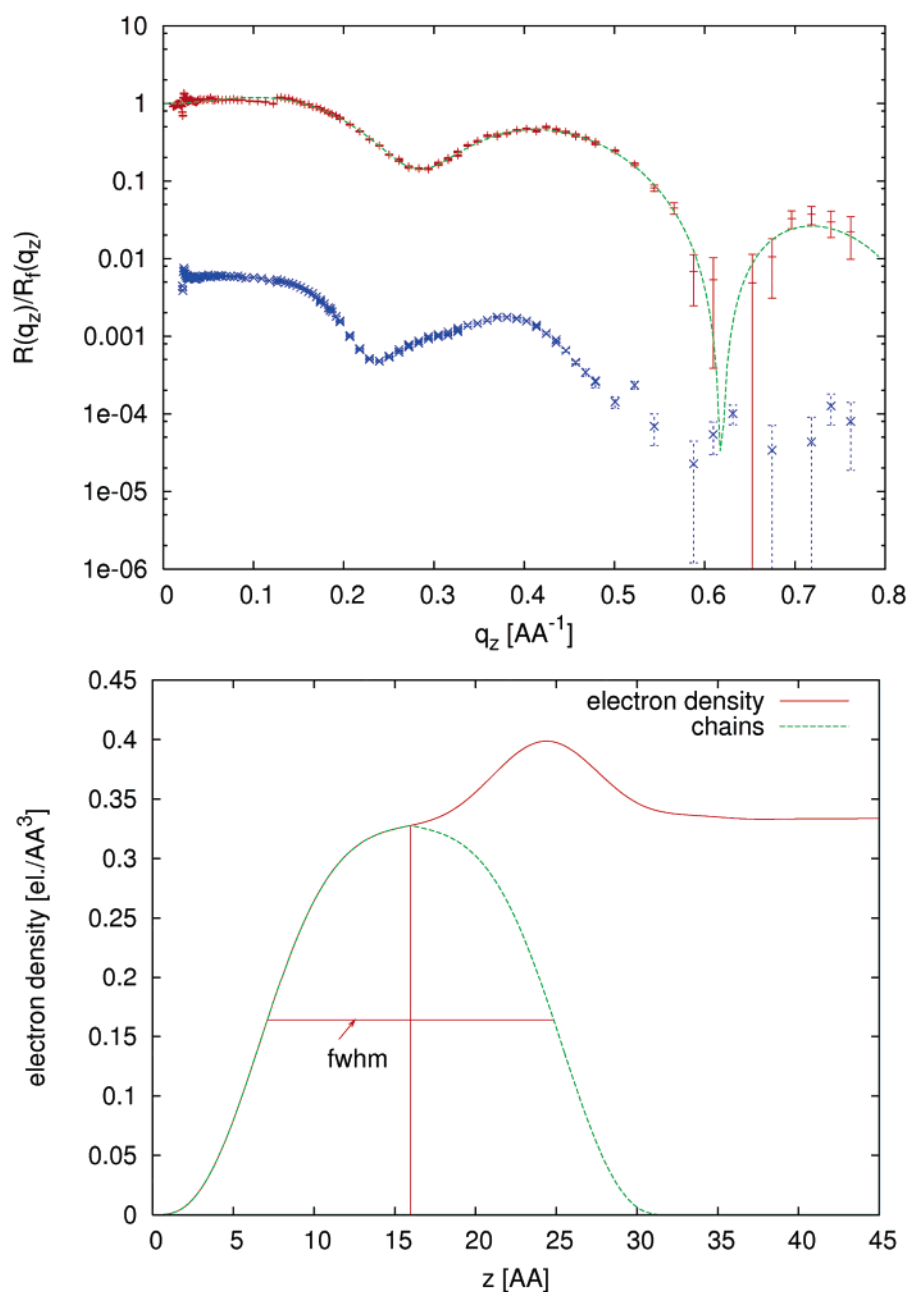

Figure 5. (Top) Specular X-ray reflectivity normalized by the Fresnel reflectivity, $R(q_z)/R_f(q_z)$, of a β-FHE monolayer measured at $\pi = 9.8$ mN/m (upper curve) and in the second plateau region (lower curve, shifted for clarity with a factor of 0.005). (Bottom) Electron density profile (red solid line) along the surface normal z. Electron density profile of the alkyl tail (green dotted line) has been calculated with the assumption of a symmetrical distribution and accounting for the number of electrons in the chain and the area per chain.

Contact Angle Measurements. Contact angle measurements using hexadecane as liquid further support the existence of "tail-to-tail" bilayer structure on mica surfaces. The static contact angle of the β-FHE monolayer (30 mN/m) is 35.3°, which is close to that of a stearic acid monolayer (30 mN/m, 36.9°). While the static contact angle of the β-FHE film deposited at
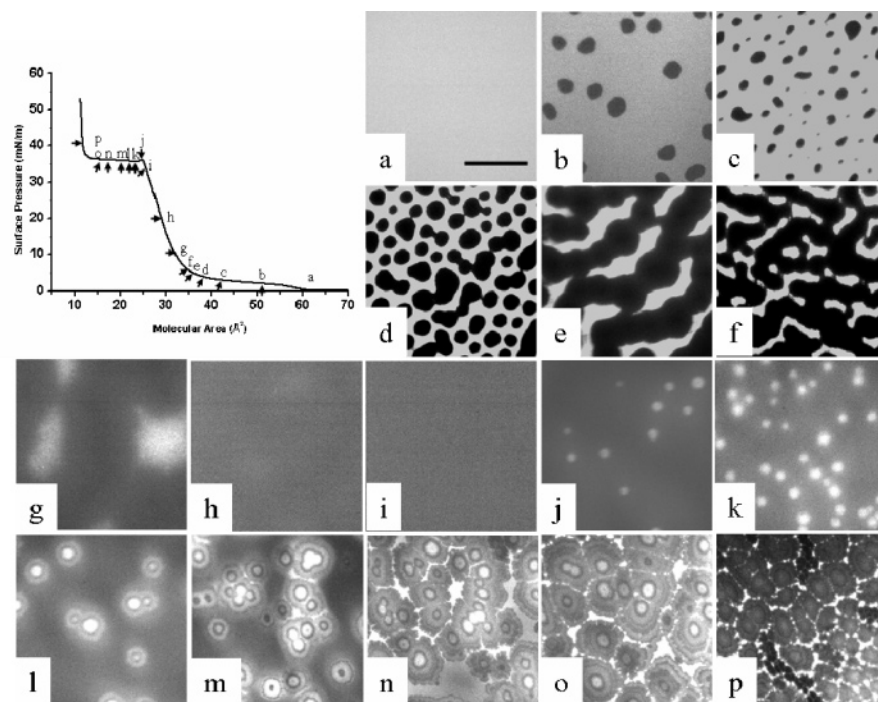
Figure 6. Typical FM images taken at various points along the isotherm at the air–water interface at 20 °C. The film contains 1 mol % fluorescence probe NBD-PC, and the scale bar for fluorescence micrographs is 50 μm.
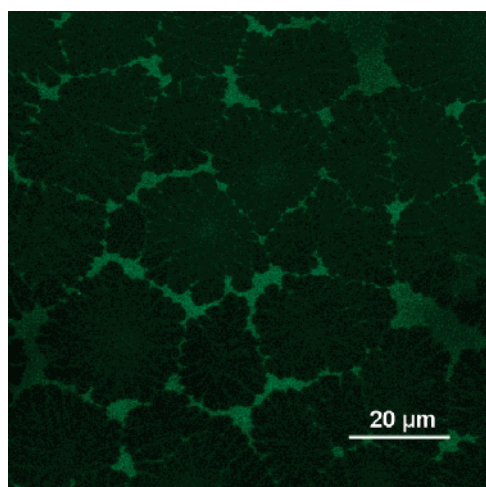

Figure 7. CLSM image of the film of β-FHE doped with 1 mol % NBD-PC transferred onto mica at the second plateau of $A = 14$ Å^2. ($\lambda_{exc} = 488$ nm, detected at 500–600 nm).

the second plateau ($^2/_3$ bilayer coverage) is 26.4°, and the static contact angle of the pure mica is 9.8°. The contact angle on the composite surface can be obtained from the Cassie equation:[28]

$$\cos\theta_c = f_1 \cos\theta_{bilayer} + f_2 \cos\theta_{monolayer}$$

where θ_c is the Cassie contact angle (i.e., 26.4° in the present case), and f_1 and f_2 are the fractional areas of the two components ($f_1 + f_2 = 1$). This expression gives the contact angle of a pure bilayer, which is 20.7°. This suggests that the surface property of the bilayer ranges between the mica and the β-FHE monolayer. In addition, a significant drop in surface potential of the surface potential–molecular area ($\Delta V - A$) isotherm is observed in the second plateau region of the $\pi - A$ isotherm, which suggests the dipoles of the second layer pointing opposite

to the first monolayer dipoles (see Supporting Information Figure S1). This result provides further experimental evidence to support the "tail-to-tail" bilayer structure in the second plateau region.

FT-IR Spectroscopic Measurements. Here, the results of FT-IR spectroscopic measurements (Figure 11) indicate the presence of hydrogen bonding in the monolayer. First of all, for the methyl octadecanoate in KBr pellet, which does not have hydrogen bonds between molecules, the C=O stretching band appears at 1742 cm^{-1}. In contrast, the C=O stretching band of β-FHE molecule in KBr pellet was 1718 cm^{-1}. It has been convincingly reported earlier that the C=O stretching band will shift toward lower wavenumbers when the carbonyl group is hydrogen bonded.[29-31] This suggests that there exist hydrogen bonds in β-FHE in solid state, while for the β-FHE multimonolayer film deposited at a surface pressure of 30 mN/m on a flat gold surface, there are two peaks at 1726 and 1741 cm^{-1}. Compared to the results of methyl octadecanoate and β-FHE in KBr pellet, the 1726 cm^{-1} band for β-FHE multimonolayer film has to be attributed to the hydrogen bonded carbonyl group, while the band at 1741 cm^{-1} belongs to a free carbonyl group. For β-FHE molecules, there are two different intermolecular hydrogen bonds resulting from interaction between a 2-hydroxyl group and a carbonyl group or a 2-hydroxyl group and a 3-fluorine group.[32] Combining the FT-IR data here, it would suggest that β-FHE molecules could form a hydrogen bonding network in the monolayer by both above-mentioned possibilities. Compression of the film causes the headgroups of β-FHE connecting together by hydrogen bonds, while the chains are free to rotate around the headgroup because of the large available space. So, the loose packing of the first layer due to the mismatch between area requirement of headgroup and chain is compensated by interdigitation of the hydrocarbon chains from the second monolayer. The interdigitation of the hydrocarbon chains in the bilayer, thereby, maximizes the hydrophobic interaction as well as hydrogen bonding interactions of the headgroups, leading to stable bilayer assemblies.
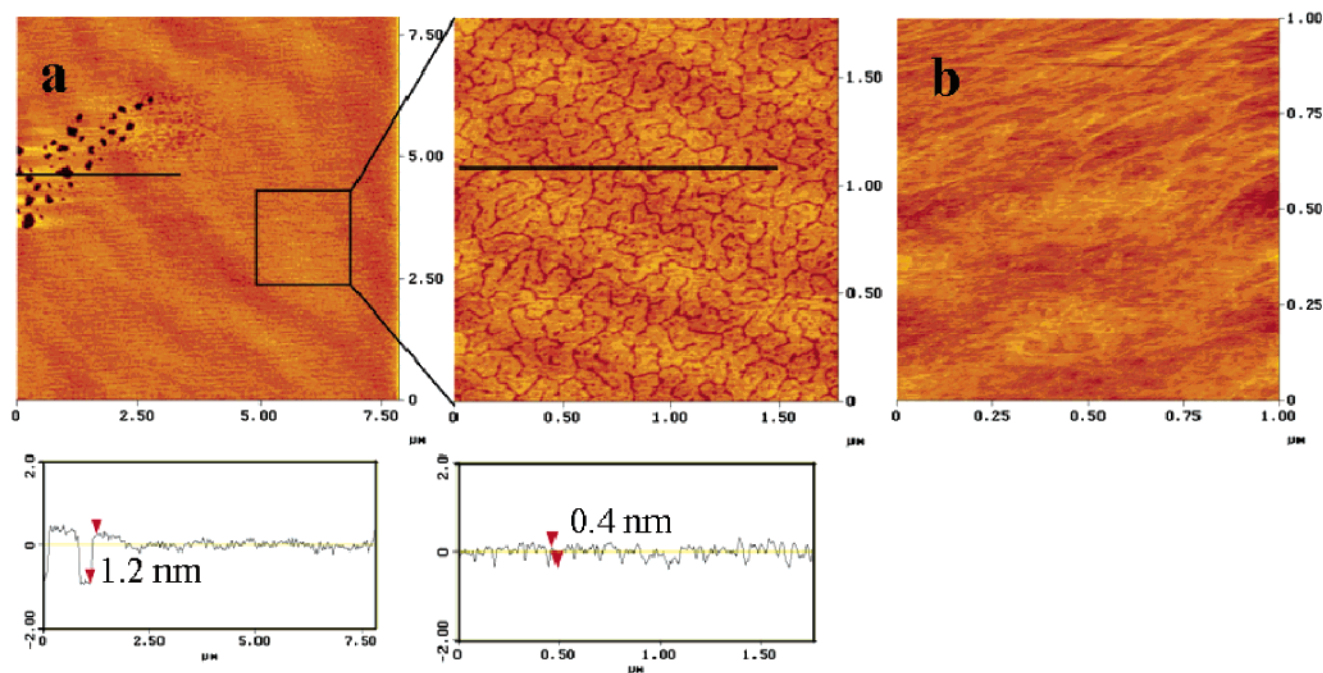
Bilayer Formed by Fatty Acid Methyl Esters

J. Phys. Chem. B, Vol. 109, No. 42, 2005 **19871**

Figure 8. AFM images of β-FHE monolayers on mica transferred at surface pressure of (a) 4 mN/m and (b) 32 mN/m.
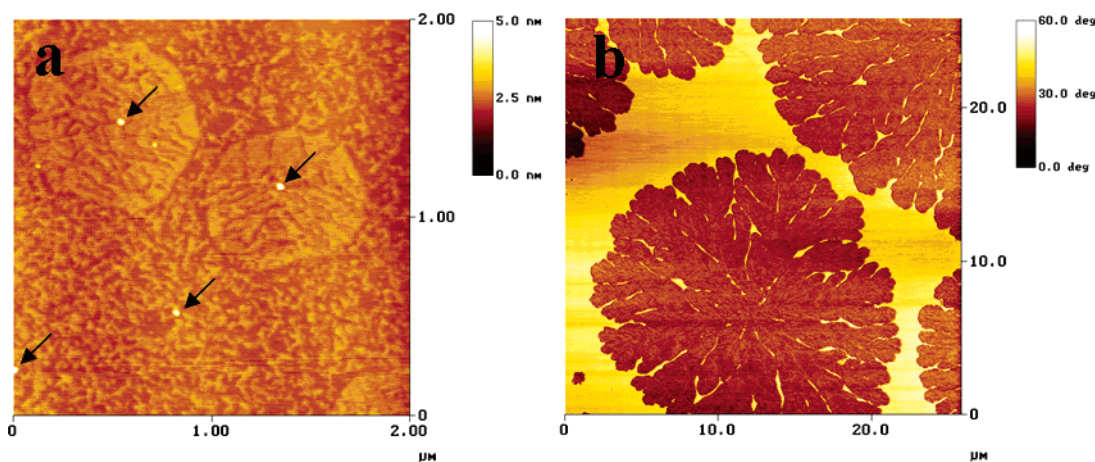

Figure 9. (a) AFM height image of the film of β-FHE doped with 1 mol % NBD-PC transferred onto mica at the beginning of second plateau crossing the inflection point. (b) AFM phase image of the film of β-FHE doped with 1 mol % NBD-PC transferred onto mica at the second plateau of $A = 23$ Å^2.

Headgroup and Chain Length Effect. We find the headgroup of β-FHE plays an important role in the bilayer formation. For the regioisomeric (2S,3S)-2-fluoro-3-hydroxyeicosanoic acid methyl ester (α-FHE), having the same length of the chain as β-FHE, only multilayer structures are obtained at the collapsed region (see Supporting Information Figure S2). The reason may be that the headgroup interaction of α-FHE is less pronounced compared to that of β-FHE.[32] Moreover, we find that the length of the chain also plays an important role; even the headgroup is identical. Racemic *anti*-3-fluoro-2-hydroxyoctadecanoic acid methyl ester (β-FHO), with a shorter by two CH$_2$ groups chain length compared to β-FHE, clearly forms interdigitated bilayer structures in the collapse region, as shown in AFM of Figure 12. We do not see clear domains (BAM of Figure 12a) before the collapse point of the isotherm. Only the flattened surface was observed in AFM measurement if we transferred the film before the collapsed point onto mica. The reason is that, before the collapsed point, only LE monolayer was formed. However, after the collapse point, big domains are formed (BAM of Figure

12b). When the domains transferred onto the mica surface are imaged by AFM, a clearly interdigitated bilayer structure with amorphous monolayer was observed. However, racemic *anti*-3-fluoro-2-hydroxyhexadecanoic acid methyl ester (β-FHH), which has a much shorter chain length (four CH$_2$ groups less) in the chain compared to β-FHE, does not form a bilayer in the collapse region (see Supporting Information Figure S3). This may be due to the less-efficient hydrophobic interactions between the chains. The long hydrocarbon chains seem to stabilize the bilayer by the van der Waals chain-to-chain attraction opposing the strong repulsion between the equally orientated dipoles of the headgroups.

Mechanism of Interdigitated Bilayer Formation. The above results proved the formation of a "tail-to-tail" interdigitated bilayer (Figure 1d and inset of Figure 2) in the second plateau region of the isotherm at the air−water interface and on the mica substrate. Now, we address the question how such interdigitated bilayer is formed from the LC monolayer upon compression. Spreading β-FHE on the water interface yields a
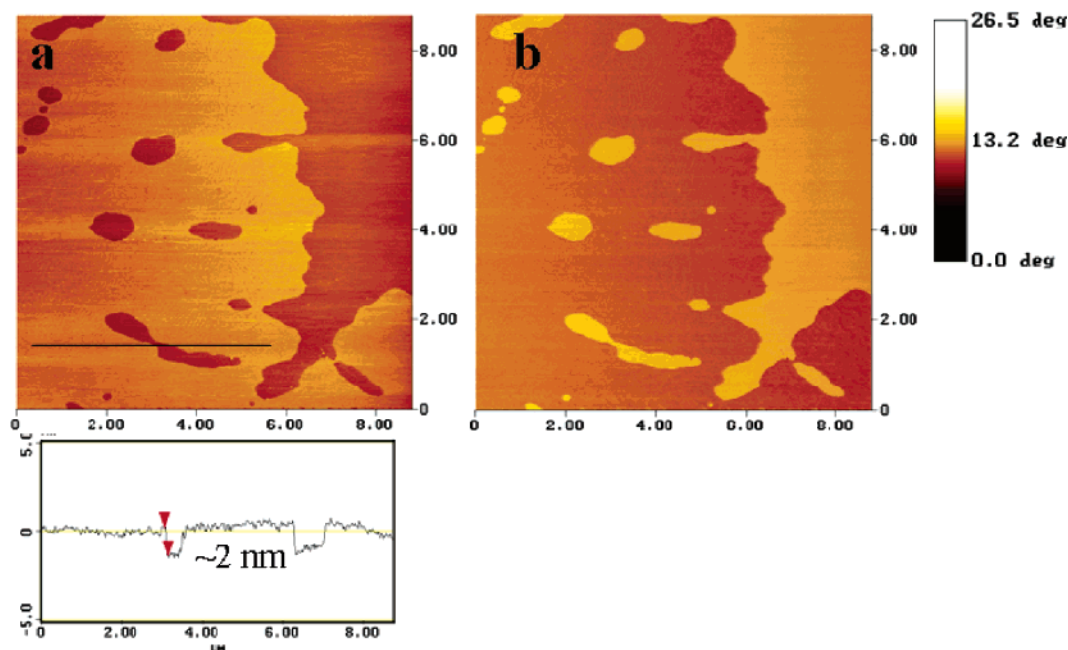
Figure 10. AFM topography image (a) and phase image (b) for the film transferred onto mica at $A = 18$ Å^2 and $\pi = 36$ mN/m. The bottom of the topography image shows the corresponding height profile.

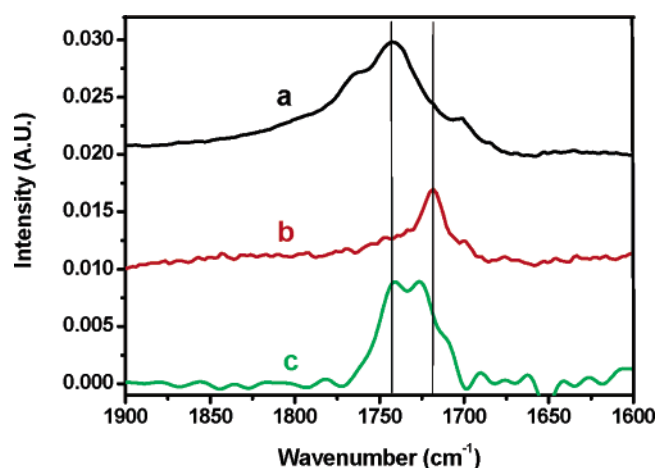**Figure 11.** FT-IR spectra of (a) methyl octadecanoate dispersed in KBr pellet, (b) β-FHE dispersed in KBr pellet, and (c) β-FHE LB multimonolayer film deposited onto a flat gold surface at the surface pressure of 30 mN/m.

m) compared to normal fatty acid methyl ester, for instance, 0° for methyl palmitate at 20 mN/m.[35] Granek et al.[36] suggested that, in the absence of molecular tilt with respect to the surface normal, a pure monolayer at the air−water interface would usually not buckle at positive. So, for the present system, the coupling between tilt and curvature associated with the head-group chain packing asymmetry might be the mechanism to giving rise to a buckling and folding of the monolayer accounts for the transition LC monolayer to bilayer.[36] Further compression of the film at the second plateau region leads to a transition from the monolayer to the interdigitated bilayer, which was confirmed by analysis of BAM, FM, and AFM measurements performed along the plateau region of the $\pi-A$ isotherm combined with the contact angle measurements. Intermolecular hydrogen bonds help to stabilize the films, and chain−chain van der Waals interactions promote the formation of the interdigitated bilayer, which means that another chain from the upper monolayer fills up the space between adjacent chains, thus minimizing the van der Waals energy.

The appearance of fractal structures of the bilayer sheds light on the mechanism of bilayer growth. Branched, dendritic patterns in interfacial growth are usually a consequence of nonequilibrium conditions at the growth interface.[37,38] The diffusion-limited aggregation (DLA),[39] which assumes an immobile cluster progressively growing by aggregation of monomeric particles with a sticking probability of unity, is the most likely mechanism corresponding to the fractal growth of bilayer at the second plateau. "Diffusion-limited" means that the monomeric particles are considered to be present in low concentrations so they do not come into contact with each other and the structure grows by adding one particle at a time rather then by adding chunks of particles. The DLA model has been successfully applied to describe fractal phenomena in various systems.[40] For our present system, the small dots in circular domains (Figure 9a) could be assumed as the nucleus of bilayer, while other small dots could act as "monomers" (Figure 9a). The growth process of the bilayer is shown in Scheme 2, where the big dot represents the nucleus and the small dots represent
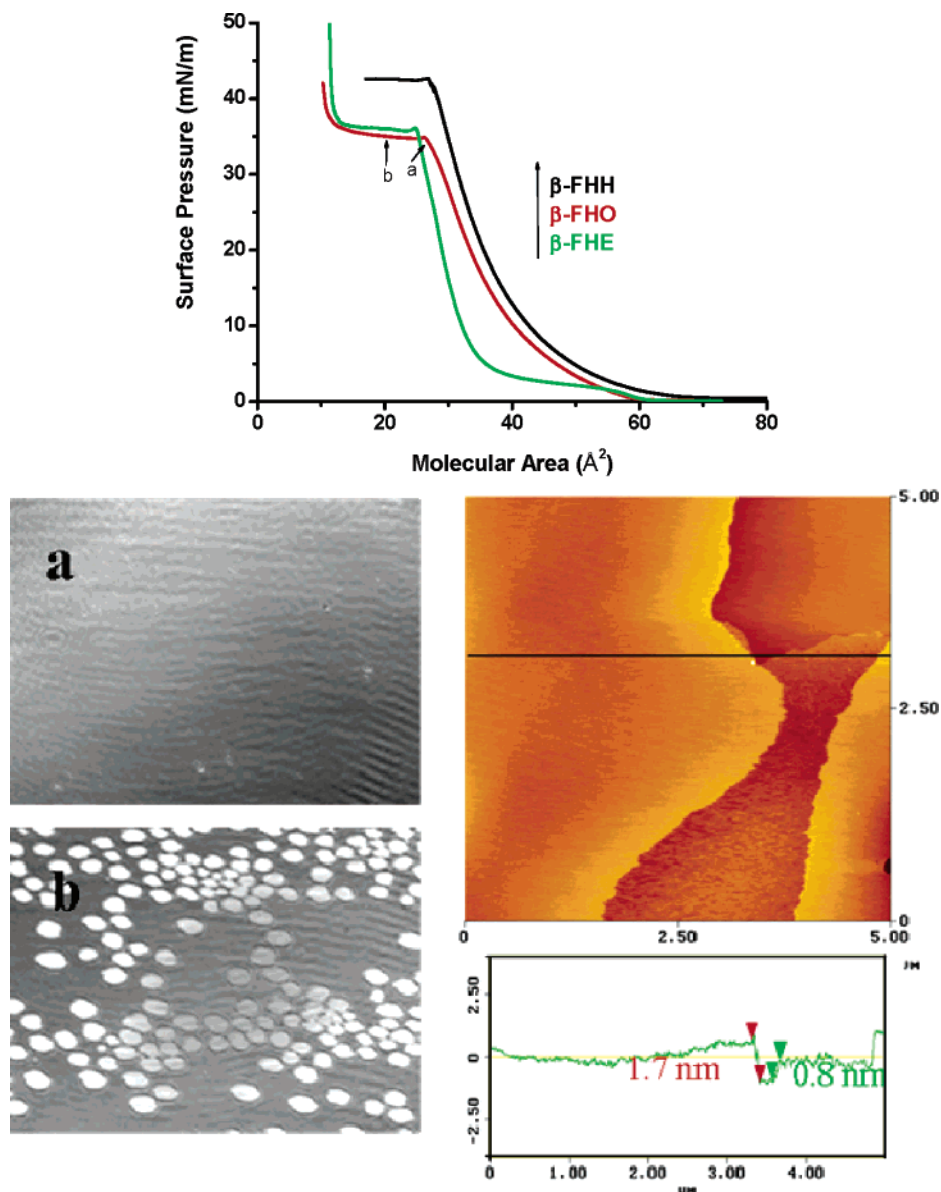
homogeneous LC monolayer formation before the second plateau. Further, a slight overcompression of the film results in an inflection point (before the turndown of the overshoot) at about $\pi = 36.4$ mN/m, before the monolayer−bilayer coexistence $\pi \sim 36$ mN/m is reached. It was reported before that a local maximum in the isotherm, that is, when $\partial\pi/\partial A = 0$, could be an indication for the buckling transition from convex to concave shape.[14] So, for our present system, the buckling modulation would be a possible process to release stress upon overcompression of the Langmuir monolayer, while the folding, which is very likely stabilized by the strong van der Waals interaction between the molecular chains, is the intermediate state for the transition from monolayer to bilayer. The collapse process is shown in Scheme 1. In the present case, the folding occurs in a one-phase region, which is in contrast to phospholipid monolayers, for which folding is observed in the phase coexistence region.[33,34] In the LC monolayer, according to GIXD and XR results, the tilt angle is much bigger (32° at ∼30 mN/

Bilayer Formed by Fatty Acid Methyl Esters

*J. Phys. Chem. B, Vol. 109, No. 42, 2005* **19873**

Figure 12. (Top) $\pi - A$ isotherms of Langmuir films of molecules with different chain length at the air−water interface at 20 °C. (Bottom) Typical BAM images for β-FHO Langmuir film before collapse and after collapse. AFM image of the Langmuir film transferred in the plateau region shows clearly the coexistence between the amorphous monolayer and the interdigitated bilayer structure.

SCHEME 1: Schematic Representations of the Collapsed Processes
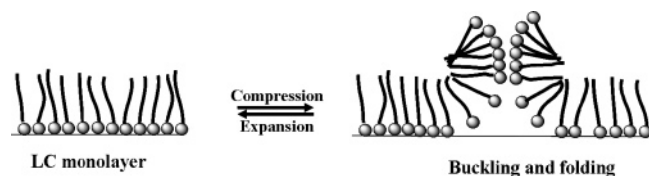
SCHEME 2: Schematic Representation of the Growth Process of Bilayer
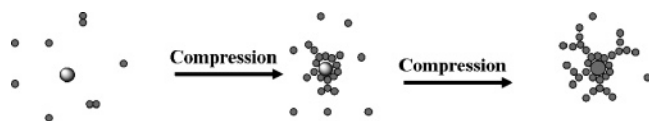
monomers. Upon compression, the "monomers" are diffused to the nucleus to form fractal structures. The continuous compression at the second plateau, i.e., progressive reducing the molecular area, implies the increasing concentration of "monomers", which leads to the fast growth of fractal structures. From FM images, we also found the transformation of fractal structures into denser structures, which can be well understood by the nucleation-growth-collision theory.[41]

Application to Understand Physiological Behaviors of Lung Surfactants. Another unconventional feature of the present system is the reversible bilayer and monolayer formation at the air−water interface, i.e., reversible collapse. No hysteresis is observed in the $\pi - A$ isotherm, and the reversible process is clearly confirmed by BAM measurements, as shown in Figure 13. It was suggested before that such a reversible collapse and the coexistence of 2D and 3D structures may play essential roles in the functioning of lung surfactants.[16,17,42] So, it seems that β-FHE is an ideal model to understand physiological behaviors of lung surfactants.

3. Conclusion

In summary, we report on an air-stable matrix (water and solid) supported interdigitated bilayer of a simple fluorinated
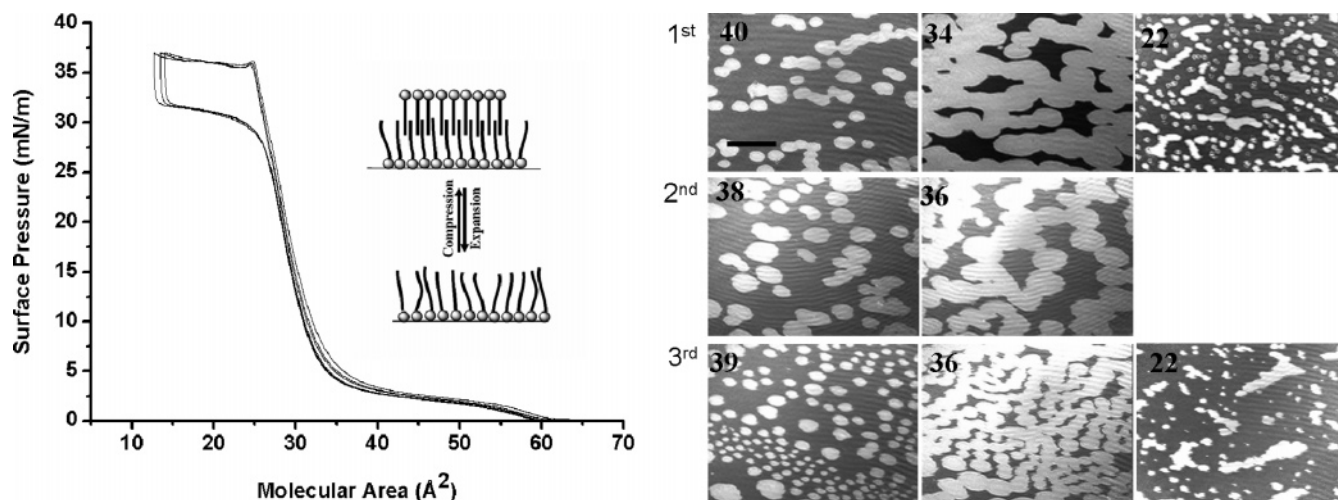
Figure 13. Hysteresis isotherms of β-FHE Langmuir film (left) and corresponding BAM images during the compression (right). The value in the BAM images represents the molecular area where the image was recorded.

hydroxyl fatty acid methyl ester formed without any substrate modification or protein inclusion. The packing incompatibility within a layer is compensated by interdigitation of the hydrocarbon chains from upper monolayer. It was suggested that the intermolecular hydrogen bonds between the headgroups and the hydrophobic interaction between chains are responsible for the stable interdigitated bilayer formation. Also, β-FHE might be a good model for mimicking the lung surfactant due to the reversible bilayer and monolayer formation at the air–water interface. Moreover, the ability of such a system to form a stable bilayer at the air–water interface and on solid substrate may enable us to probe its use as a matrix in biosensing.

4. Experimental Section

Materials. The synthesis of a series of 2,3-disubstituted methyl alkanoates has been described elsewhere.[24,43] The fluorescence probe, 2-(12-(7-nitrobenz-2-oxa-1,3-diazol-4-yl)-amino)dodecanoyl-1-hexadecanoyl-*sn*-glycero-3-phosphocholine (NBD-PC), was purchased from Molecular Probes (Leiden, Netherlands). All substances were dissolved in chloroform (HPLC grade) purchased from AppliChem (Darmstadt, Germany). Stearic acid and hexadecane were purchased from Sigma and used without further purification.

Isotherms Measurement. π–A isotherms were recorded on a Teflon trough (NIMA, Coventry, UK) with total surface area of 690 cm^2. The surface pressure was measured with a Wilhelmy plate system. The water (18.2 MΩ·cm) was obtained from a Millipore purification system. The chloroform solutions of the substances were spread with a microsyringe onto the water surface, and the films were then equilibrated for 15 min before compression. The compression rate was 10 cm^2/min, and the subphase temperature was kept at 20 °C. For the collapse pressure depending on compression rate, the isotherms were recorded on a commercial Langmuir film balance (NIMA 6100) with total surface area of 260 cm^2.

Brewster Angle Microscopy. The monolayers were visualized by a Brewster angle microscope (BAM 2Plus, Nanofilm Technologie GmbH, Göttingen, Germany) mounted on the NIMA trough. The light source of the BAM was an Nd:YAG laser. The laser beam is reflected at the air–water interface at the Brewster angle. The reflected beam is recorded with a CCD camera, and the data were digitally saved. The 10× objective provides a diffraction limited lateral resolution of approximately 2 μm. The size of BAM images in this paper is 430 × 537 μm^2.

Fluorescence Microscopy (FM). For the fluorescence microscopy investigations, the film balance (144 cm^2, Riegler & Kirstein) was mounted onto the stage of the Olympus microscope BX-FLA (Hamburg, Germany) equipped with a mercury lamp (USH-102D 100 W, power supply unit BH2-RFL-T3), an objective (LMPLFL 50×), and a CCD camera with a camera controller (Hamamatsu C4742-95, Hamamatsu, Japan). The spreading solutions contained 1 mol % fluorescence probe NBD-PC.

Langmuir–Blodgett (LB) Film Deposition. A commercial Langmuir film balance (NIMA 6100) was used to transfer the Langmuir film onto a solid substrate at a constant pressure with a dipping speed of 5 mm/min. For AFM measurement, freshly cleaved mica (Plano, Germany) was thoroughly rinsed with Milli-Q water and used as supporting solid substrate. While for the IR measurement, freshly Au(200 nm)/Cr(10 nm) covered glass plates were used as a substrate.

Atomic Force Microscopy. AFM inspections were performed with a commercial instrument (Digital Instruments, Nanoscope IIIa, Dimension 3000) running in tapping mode (Si cantilevers (Nanosensors) of spring constants 250–350 kHz).

Grazing Incidence X-ray Diffraction and X-ray Reflectivity. The GIXD and XR experiments on Langmuir films were performed on the liquid surface diffractometer installed at the synchrotron undulator beamline BW1 in HASYLAB, DESY (Hamburg, Germany). The experimental setup and evaluation procedures are described in detail elsewhere.[44,45] The dimensions of the footprint of the incoming X-ray beam on the liquid surface were approximately 2 × 50 mm^2. The X-ray beam with a wavelength $\lambda = 1.304$ Å was made monochromatic by Bragg reflection at the (002) plane of a beryllium crystal. It hit the air–water interface at a grazing incidence angle $\alpha_i = 0.85\alpha_c$, where α_c is the critical angle ($\approx 0.13°$) for total external reflection. The intensity of the diffracted beam is detected by a position-sensitive detector (PSD) (OED-100-M, Braun, Garching, Germany). The resolution (1.5 mrad) of the horizontal scattering angle $2\theta_{hor}$ was given by a Soller collimator located in front of the PSD. The scattering vector Q had an in-plane component $Q_{xy} \approx 2k \sin(\theta_{hor})$ and an out-of-plane component $Q_z \approx -k \sin(\alpha_f)$, where $k = 2\pi/\lambda$ is the wave vector and α_f is the vertical scattering angle. The measurements were performed by scanning across the in-plane component Q_{xy} and simultaneously resolving the out-of-plane component Q_z with the PSD. The accumulated position-resolved scans were corrected for

Bilayer Formed by Fatty Acid Methyl Esters

J. Phys. Chem. B, Vol. 109, No. 42, 2005 **19875**

polarization, footprint area, and powder-averaging (Lorentz factor). Model peaks taken to be Lorentzian in the in-plane direction and Gaussian in the out-of-plane direction were fitted to the corrected intensities. From the peak positions, we can obtain the lattice parameters and the tilt angle t. The cross-sectional area of the chains is given by $A_0 = A_{xy} \cos(t)$.

The specular X-ray reflectivity (XR) data collection was performed by using a NaI scintillation detector. The X-ray reflectivity was measured as a function of the vertical incidence angle, α_i, with the geometry, $\alpha_i = \alpha_f = \alpha$, where α_f is the vertical exit angle of the reflected X-rays. An X-ray wavelength of $\lambda = 1.304$ Å was used. XR data were collected as a function of the incidence angle, α_i, varied in the range $0.05-5°$, corresponding to a range $0.01-0.85$ Å^{-1} of the vertical scattering vector component $q_z = (4\pi/\lambda) \sin(\alpha)$. The background scattering from, e.g., the subphase was measured at $2\theta_{hor} = 0.7°$ and subtracted from the signal measured at $2\theta_{hor} = 0$. The X-ray footprint area on the sample is inversely proportional to the incident angle of the X-rays. The reflectivity data were inverted by applying a model-independent approach.[23] Subsequently, the obtained electron density profile was chemically interpreted by applying prior information such as surface area of the molecule. Assuming the tail group to be symmetric and constraining the number of electrons in tails results in a unique electron density distribution for the tails.

Confocal Laser Scanning Microscope. CLSM Fluorescent images were acquired with commercial confocal laser scanning microscope (Leica TCS SL, Heidelberg, Germany), equipped with a $63\times$ oil immersion objective with a numerical aperture of 1.32 and Ar laser excitation.

Contact Angle Measurement. Contact angle measurements were made by using a contact angle measuring system G2 (Krüss, Germany) with sessile drop method. Static angles were recorded when the probe fluid, hexadecane, was added to substrate. The values reported are averages of at least three measurements made on different areas of the sample surface.

FT-IR Spectra. The FT-IR spectra of the molecules dispersed in KBr pellet was recorded by a Perkin-Elmer 1600 Series FT-IR. β-FHE multimonolayer LB film that was deposited onto the Au(200 nm)/Cr(10 nm) glass plate by using the vertical lifting method at 30 mN/m and 20 °C was recorded by a JASCO FT-IR 660 spectrometer.

Supporting Information Available: The $\Delta V-A$ isotherm of β-FHE Langmuir film, $\pi-A$ isotherm and the hysteresis isotherm of α-FHE Langmuir film, BAM and AFM images of α-FHE and β-FHH Langmuir film at the collapse plateau region. This material is available free of charge via the Internet at http://pubs.acs.org.

References and Notes

(1) Brian, A. A.; McConnell, H. M. *Proc. Natl. Acad. Sci. U.S.A.* **1984**, *81*, 6159−6163.

(2) Sackmann, E. *Science* **1996**, *271*, 43−48.

(3) Bayley, H.; Cremer, P. S. *Nature* **2001**, *413*, 226−230.

(4) Anrather, D.; Smetazko, M.; Saba, M.; Alguel, Y.; Schalkhammer, T. *J. Nanosci. Nanotechnol.* **2004**, *4*, 1−22.

(5) Plant, A. L. *Langmuir* **1999**, *15*, 5128−5135.

(6) Conboy, J. C.; Liu, S. C.; O'Brien, D. F.; Saavedra, S. S. *Biomacromolecules* **2003**, *4*, 841−849.

(7) Ross, E. E.; Bondurant, B.; Spratt, T.; Conboy, J. C.; O'Brien, D. F.; Saavedra, S. S. *Langmuir* **2001**, *17*, 2305−2307.

(8) Ross, E. E.; Rozanski, L. J.; Spratt, T.; Liu, S. C.; O'Brien, D. F.; Saavedra, S. S. *Langmuir* **2003**, *19*, 1752−1765.

(9) Fang, Y.; Frutos, A. G.; Lahiri, J. *J. Am. Chem. Soc.* **2002**, *124*, 2394−2395.

(10) Holden, M. A.; Jung, S. Y.; Yang, T. L.; Castellana, E. T.; Cremer, P. S. *J. Am. Chem. Soc.* **2004**, *126*, 6512−6513.

(11) Wetzer, B.; Pum, D.; Sleytr, U. B. *J. Struct. Biol.* **1997**, *119*, 123−128.

(12) Kuzmenko, I.; Rapaport, H.; Kjaer, K.; Als-Nielsen, J.; Weissbuch, I.; Lahav, M.; Leiserowitz, L. *Chem. Rev.* **2001**, *101*, 1659−1696.

(13) Kuzmenko, I.; Buller, R.; Bouwman, W. G.; Kjaer, K.; AlsNielsen, J.; Lahav, M.; Leiserowitz, L. *Science* **1996**, *274*, 2046−2049.

(14) Kuzmenko, I.; Kindermann, M.; Kjaer, K.; Howes, P. B.; Als-Nielsen, J.; Granek, R.; von Kiedrowski, G.; Leiserowitz, L.; Lahav, M. *J. Am. Chem. Soc.* **2001**, *123*, 3771−3783.

(15) Xue, J. Z.; Jung, C. S.; Kim, M. W. *Phys. Rev. Lett.* **1992**, *69*, 474−477.

(16) Galla, H.-J.; Malcharek, S.; Bourdos, N. In *Lung Surfactant Function and Disorder*; Nag, K. Ed.; Taylor & Francis Group: Boca Raton, FL, 2005, pp 251−274.

(17) Schurch, S.; Green, F. H. Y.; Bachofen, H. *Biochim. Biophys. Acta* **1998**, *1408*, 180−202.

(18) Kwok, D. Y.; Tadros, B.; Deol, H.; Vollhardt, D.; Miller, R.; CabrerizoVilchez, M. A.; Neumann, A. W. *Langmuir* **1996**, *12*, 1851−1859.

(19) Adams, J.; Buske, A.; Duran, R. S. *Macromolecules* **1993**, *26*, 2871−2877.

(20) Rapp, B.; Gruler, H. *Phys. Rev. A* **1990**, *42*, 2215−2218.

(21) Kampf, J. P.; Frank, C. W.; Malmstrom, E. E.; Hawker, C. J. *Science* **1999**, *283*, 1730−1733.

(22) Gourier, C.; Knobler, C. M.; Daillant, J.; Chatenay, D. *Langmuir* **2002**, *18*, 9434−9440.

(23) Pedersen, J. S.; Hamley, I. W. *J. Appl. Crystallogr.* **1994**, *27*, 36−49.

(24) Wiehle, S.; Grimme, S.; Haufe, G. *Eur. J. Org. Chem.* **2005**, submitted.

(25) Chi, L. F. *Appl. Phys. A* **1999**, *68*, 203-210.

(26) Gao, S.; Chi, L. F.; Lenhert, S.; Anczykowski, B.; Niemeyer, C. M.; Adler, M.; Fuchs, H. *ChemPhysChem* **2001**, *2*, 384−388.

(27) Chi, L. F.; Jacobi, S.; Anczykowski, B.; Overs, M.; Schäfer, H. J.; Fuchs, H. *Adv. Mater.* **2000**, *12*, 25−30.

(28) Adamson, A. W.; Gast, A. P. *Physical Chemistry of Surfaces*; John Wiley and Sons: New York, 1997.

(29) Huo, Q.; Dziri, L.; Desbat, B.; Russell, K. C.; Leblanc, R. M. *J. Phys. Chem. B* **1999**, *103*, 2929−2934.

(30) Huo, Q.; Russev, S.; Hasegawa, T.; Nishijo, J.; Umemura, J.; Puccetti, G.; Russell, K. C.; Leblanc, R. M. *J. Am. Chem. Soc.* **2000**, *122*, 7890−7897.

(31) Koyano, H.; Bissel, P.; Yoshihara, K.; Ariga, K.; Kunitake, T. *Chem.—Eur. J.* **1997**, *3*, 1077−1082.

(32) Chen, X. D.; Wiehle, S.; Chi, L. F.; Mück-Lichtenfeld, C.; Rudert, R.; Vollhardt, D.; Fuchs, H.; Haufe, G. *Langmuir* **2005**, *21*, 3376−3383.

(33) Lipp, M. M.; Lee, K. Y. C.; Takamoto, D. Y.; Zasadzinski, J. A.; Waring, A. J. *Phys. Rev. Lett.* **1998**, *81*, 1650−1653.

(34) Gopal, A.; Lee, K. Y. C. *J. Phys. Chem. B* **2001**, *105*, 10348−10354.

(35) Weidemann, G.; Brezesinski, G.; Vollhardt, D.; Bringezu, F.; de Meijere, K.; Möhwald, H. *J. Phys. Chem. B* **1998**, *102*, 148−153.

(36) Hu, J. G.; Granek, R. *J. Phys. II* **1996**, *6*, 999−1022.

(37) Benjacob, E.; Garik, P. *Nature* **1990**, *343*, 523−530.

(38) Gehlert, U.; Vollhardt, D. *Langmuir* **1997**, *13*, 277−282.

(39) Witten, T. A.; Sander, L. M. *Phys. Rev. Lett.* **1981**, *47*, 1400−1403.

(40) Vicsek, T. *Fractal Growth Phenomena*; World Scientific: Singapore, 1992.

(41) Vollhardt, D.; Ziller, M.; Retter, U. *Langmuir* **1993**, *9*, 3208−3211.

(42) Warriner, H. E.; Ding, J.; Waring, A. J.; Zasadzinski, J. A. *Biophys. J.* **2002**, *82*, 835−842.

(43) Wiehle, S. Ph.D. Thesis, University of Münster, Münster, Germany, 2004.

(44) Als-Nielsen, J.; Jacquemain, D.; Kjaer, K.; Leveiller, F.; Lahav, M.; Leiserowitz, L. *Phys. Rep.* **1994**, *246*, 252−313.

(45) Kjaer, K. *Physica B* **1994**, *198*, 100−109.